Check for updates

AGU ADVANCING EARTH AND SPACE SCIENCES

Water Resources Research

RESEARCH ARTICLE
10.1029/2023WR035064

# Rapid Permeability Upscaling of Digital Porous Media via Physics-Informed Neural Networks

**Mohamed Elmorsy[1], Wael El-Dakhakhni[1,2], and Benzhong Zhao[1]**

[1]Department of Civil Engineering, McMaster University, Hamilton, ON, Canada, [2]School of Computational Science & Engineering, McMaster University, Hamilton, ON, Canada

**Key Points:**

- We derive a novel analytical solution that approximates the permeability of a three-dimensional (3D) digital rock consisting of $2 \times 2 \times 2$ anisotropic cells
- We develop physics-informed neural network (PINN) models that incorporate the analytical solution for accurate permeability upscaling
- The PINN model, when applied in concert with a 3D convolutional neural network model, achieves rapid, accurate permeability prediction of large digital rock samples

**Correspondence to:**
B. Zhao,
robinzhao@mcmaster.ca

**Citation:**
Elmorsy, M., El-Dakhakhni, W., & Zhao, B. (2023). Rapid permeability upscaling of digital porous media via physics-informed neural networks. *Water Resources Research*, *59*, e2023WR035064. https://doi.org/10.1029/2023WR035064

Received 13 APR 2023
Accepted 28 NOV 2023

© 2023 The Authors.
This is an open access article under the terms of the Creative Commons Attribution-NonCommercial License, which permits use, distribution and reproduction in any medium, provided the original work is properly cited and is not used for commercial purposes.

**Abstract** Subsurface processes are important in solving many of the grand challenges facing our society today, including the sustainable extraction of hydrocarbons, the permanent geological sequestration of carbon dioxide, and the seasonal storage of renewable energy underground. Permeability characterization of underground rocks is the critical first step in understanding and engineering these processes. While recent advances in machine learning methods have enabled fast and efficient permeability prediction of digital rock samples, their practical use remains limited since they can only accommodate subsections of the digital rock samples, which is often not representative of properties at the core-scale. Here, we derive a novel analytical solution that approximates the effective permeability of a three-dimensional (3D) digital rock consisting of $2 \times 2 \times 2$ anisotropic cells based on the physical analogy between Darcy's law and Ohm's law. We further develop physics-informed neural network (PINN) models that incorporate the analytical solution and subsequently demonstrate that the PINN equipped with the physics-informed module achieves excellent accuracy, even when used to upscale previously unseen samples over multiple levels of upscaling. Our work elevates the potential of machine learning models such as 3D convolutional neural network for rapid, end-to-end digital rock analysis at the core-scale.

## 1. Introduction

Many natural and industrial processes involve subsurface fluid flow, including groundwater hydrology (Bear, 2013; Freeze & Cherry, 1979), energy extraction (Lake, 1989; Orr & Taber, 1984), geological storage of carbon dioxide and hydrogen (Heinemann et al., 2021; Szulczewski et al., 2012). Permeability, which measures the ease with which fluids pass through a porous medium, is a fundamental parameter governing fluid flow in the subsurface. Traditionally, permeability is measured by flowing a pressurized gas or liquid through a core sample extracted from underground drilling (Bear & Bachmat, 1991). However, laboratory permeability characterization is complex and time-consuming, and it requires the use of specialized and highly calibrated equipment. Recent advances in three-dimensional (3D) imaging technologies such as X-ray micro-computed tomography (micro-CT) have enabled the creation of digital twins of core samples, which can then be used for permeability characterization (Andrä et al., 2013; Berg et al., 2017; Spanne et al., 1994).

The current benchmark for digital permeability characterization is achieved through high-resolution computational fluid dynamics (CFD) simulation of single-phase flow through digital rock samples, which provides accurate predictions for a variety of rock types, including sandstones, limestones, and carbonates (Blunt et al., 2013; Boek & Venturoli, 2010; Chen & Doolen, 1998; Dong & Blunt, 2009; Manwart et al., 2002; Mostaghimi et al., 2013). However, due to the exorbitant computational cost in terms of memory and processing time, digital permeability characterization via high-resolution CFD simulation is still limited to samples typically smaller than the representative elementary volume (REV). Even with the application of parallel computing, direct numerical simulation of flow in 3D porous media is still computationally expensive (Wang et al., 2019). For example, a 5 $mm^3$ carbonate core sample is thought to require $\sim 10^{13}$ grid cells to simulate (Blunt et al., 2013). Therefore, existing direct numerical simulations are limited to studying subsections of core samples, whose permeabilities exhibit a large amount of scatter due to the small-scale heterogeneities of natural porous media.

More recently, advances in 3D convolutional neural networks (CNNs) have enabled end-to-end permeability prediction of digital rock samples with great accuracy, generalizability, and efficiency (Alqahtani et al., 2021; Elmorsy et al., 2022). However, the size of the digital samples that 3D CNNs can predict remains very small,

since their training data is derived from high-resolution CFD simulations. Therefore, alternative more efficient methods are needed to predict the permeability of digital rock samples at the core-scale (Tahmasebi et al., 2020).

One way to reduce the computational demand is *downscaling* the high-resolution images and perform direct numerical simulations on a low-resolution domain. However, this approach has been shown to miss key micro-structure information, leading to erroneous results (Zhang et al., 2022). Pore network modeling of permeability is another example of downscaling, whereby the complex 3D pore geometry is idealized as a lattice of connected pores and throats (Blunt, 2001, 2017). In general, permeability prediction obtained from pore network modeling is less accurate than direct numerical simulation due to ambiguities involved in network extraction (Dong & Blunt, 2009). An alternative approach to downscaling is *upscaling*, where one combines permeabilities obtained from fine-scale simulations on smaller subsections that are computationally tractable to predict the bulk permeability of the larger domain. Homogenization is a commonly used method in upscaling, which predicts the effective property of a slowly varying macroscopic medium based on its complex, rapidly varying microscopic constituents.

Permeability upscaling has been studied extensively in the past decades. Cardwell and Parsons (1945) found that in general, the effective permeability of a block of porous media partitioned into smaller sub-blocks with different permeabilities ranges from the harmonic and arithmetic average of the permeabilities of the sub-blocks. King (1989) conducted upscaling by representing a simple porous medium consisting of $2 \times 2$ *isotropic* sub-blocks with different permeabilities as an equivalent resistor network, taking advantage of the similarity between fluid movement through porous media and electric current flow through electric circuits, since single-phase Darcy's law shares the same mathematical formulation as Ohm's law. This equivalent resistor network is then reduced to a single resistor, whose resistance represents the inverse of the porous medium's effective permeability. In 2D, this approach results in a closed-form formula for the block permeability. Therefore, the permeability of a 2D square domain consisting of $2^n$ sub-blocks can be calculated by recursively applying the formula for upscaling $2 \times 2$ sub-blocks. This elegant approach to upscaling is often referred to as renormalization.

However, for the simplest 3D block, which consists of $2 \times 2 \times 2$ isotropic sub-blocks, King (1989) could only provide a graphical representation of the resistor network, and they stated that upscaling in 3D does not result in a simple closed-form expression. Green and Paterson (2007) developed an approximate analytical formula to this problem by representing the 3D block as four $2 \times 2$ blocks. The effective permeabilities of the $2 \times 2$ blocks were calculated using King (1989)'s formula, and the effective permeability of the 3D block was approximated as the arithmetic mean of the four $2 \times 2$ blocks. Similarly, Karim and Krabbenhoft (2010) provided an approximate analytical solution to the problem by first calculating the effective permeabilities of the four $2 \times 1$ sub-blocks in series and the two $2 \times 2$ sub-blocks in parallel. The effective permeability of the 3D block is given by the geometric mean of the effective permeabilities of the sub-blocks in series and the sub-blocks in parallel.

Bashtani et al. (2018) evaluated the effective permeability of four synthetic porous media samples based on the permeabilities of the eight $2 \times 2 \times 2$ sub-blocks using Karim and Krabbenhoft (2010)'s approximate analytical solution. The upscaled permeabilities had errors ranging from 2.7% to 11.5% compared to those acquired directly from pore network modeling. They noted that the error grows as the sample becomes more heterogeneous. More recently, Zhang et al. (2022) calculated the effective permeabilities of three digital carbonate rock samples (each consisting of eight sub-blocks) using Karim and Krabbenhoft (2010)'s analytical solution, which yielded predictions that had relative errors in the range of ~40% when compared to the permeabilities obtained from pore network modeling. To increase the prediction accuracy, they took sub-samples of each carbonate sample and related the predictions of the analytical solution to those of pore network modeling via a simple first-order linear regression model. They subsequently used this model to improve the analytical predictions of the full-size carbonate samples. However, they highlighted the fact that the process of generating the required data to fit the regression models consumed significant amount of computation time. Furthermore, this approach is not a generalizable, since a separate regression model is needed for each rock sample.

By using a different approach, Menke et al. (2021) combined machine learning with numerical simulation and informed structural analysis to upscale the permeability of heterogeneous porous media. Specifically, they introduced a machine learning-based multivariate structural regression model and predicted the permeability of limestone subvolumes of $360 \times 360 \times 360$ cubic voxel in size using the permeabilities of smaller subvolumes of $60 \times 60 \times 60$ and $120 \times 120 \times 120$ cubic voxel in size. The permeabilities of the smaller subvolumes were predicted by a multivariate regression model trained with 18 structural features extracted from micro-CT images. The predicted permeabilities of the subvolumes are then fed to a Darcy-Brinkman-Stokes model to calculate the effective permeability of the larger



19447973, 2023, 12, Downloaded from https://agupubs.onlinelibrary.wiley.com/doi/10.1029/2023WR035064 by Cochrane Canada Provision, Wiley Online Library on [28/12/2023]. See the Terms and Conditions (https://onlinelibrary.wiley.com/terms-and-conditions) on Wiley Online Library for rules of use; OA articles are governed by the applicable Creative Commons License

19447973, 2023, 12, Downloaded from https://agupubs.onlinelibrary.wiley.com/doi/10.1029/2023WR035064 by Cochrane Canada Provision, Wiley Online Library on [28/12/2023]. See the Terms and Conditions (https://onlinelibrary.wiley.com/terms-and-conditions) on Wiley Online Library for rules of use; OA articles are governed by the applicable Creative Commons License

**Table 1**
*Digital Rock Samples Used to Develop the Upscaling Methods*

| Rock type | Size (voxels) | Resolution (μm/voxel) | Porosity (–) | Stride (voxel) | Number of subvolumes (–) | Number of labeled permeabilies (–) |
|---|---|---|---|---|---|---|
| Bentheimer sandstone | $1{,}000^3$ | 3 | 0.22 | 50 | 1,704 | 5,112 |
| Ketton limestone | $1{,}000^3$ | 3 | 0.13 | 50 | 1,704 | 5,112 |
| Berea sandstone | $712^3$ | 3 | 0.19 | 50 | 1,704 | 5,112 |

$360 \times 360 \times 360$ cubic voxel samples. They found that the machine learning regression model significantly outperformed a fitted Kozeny-Carman model. Specifically, the relative mean square error (RMSE) of the Kozeny-Carman models's predictions was 29.7% while the machine learning regression model's predictions had an RMSE of 4.3%.

In another study, Siavashi et al. (2022) combined CNNs and continuum-scale simulations to upscale permeability from low-resolution images. Specifically, high-resolution images of Fontainebleau sandstone samples with labeled permeabilities were down-sampled to train a CNN. The trained CNN was then used to predict the permeabilities of low-resolution subvolumes $80 \times 80 \times 80$ cubic voxels in size. Finally, a commercial reservoir simulator was used to perform a continuum-scale simulation of the reconstructed low-resolution model that utilizes the permeabilities predicted by the CNN. The CNN's permeability prediction achieved coefficient of determination $R^2 = 0.99$ on the $80 \times 80 \times 80$ cubic voxel subvolumes, while the bulk permeability predicted by the continuum-scale simulation and direct numerical simulation on the low resolution images achieved relative errors of 1.63% and 97.27%, respectively, when compared to the results obtained from direct numerical simulation on the high-resolution images.

To address the drawbacks of existing upscaling approaches including the high computational cost associated with direct numerical simulations (Siavashi et al., 2022; Xu et al., 2022), the inaccuracies associated with pore network modeling (Dong & Blunt, 2009) and approximate analytical solutions (Wei et al., 2019), the existing literature clearly illustrates the need for an efficient, reliable, and accurate upscaling technique. We hypothesize that combining analytical methods with advanced machine-learning algorithms will significantly improve the accuracy of upscaling beyond that of approximate analytical solutions or traditional regression-based machine-learning models. Meanwhile, the ability to provide rapid predictions (less than a second) is another key advantage over upscaling methods that require direct numerical simulations (hours to days). Furthermore, this approach will expand the utility of current machine learning models for permeability prediction to larger sample sizes. For example, our previous work (Elmorsy et al., 2022) introduced an advanced 3D CNN model that provides accurate permeability prediction of digital rock samples in milliseconds. However, these predictions are limited to subsamples of size $150 \times 150 \times 150$ cubic voxels, which is often smaller than the REV of the sample. Therefore, the development of a fast and accurate upscaling technique will enable permeability prediction of digital rocks of REV size in real time.

Here, we introduce a novel analytical solution based on the physical analogy between Darcy's law and Ohm's law to approximate the upscaled permeability of $2 \times 2 \times 2$ subsample systems, where each subsample is *anisotropic*. We then integrate the analytical solution with machine learning algorithms to train two physics-informed neural network (PINN) models with hybrid learning schemes for permeability upscaling. We show the PINN models achieve rapid permeability upscaling with accuracy beyond that of the analytical solution. Finally, we demonstrate that the permeabilities of larger $600 \times 600 \times 600$ cubic voxel sandstone and carbonate samples can be accurately predicted by first dividing them into smaller $150 \times 150 \times 150$ cubic voxel subsamples, applying a 3D CNN to obtain the permeability of the subsamples, and then recursively applying the upscaling model to predict the bulk permeability of the larger samples. Therefore, our model paves the way to real time, end-to-end permeability prediction of digital porous media at the core-scale and beyond.

## 2. Materials and Methods

### 2.1. Data Preparation and Processing

We use a publicly available set of 3D images of different rock samples to develop the PINN permeability upscaling model (Table 1). These images were previously captured by Imperial College London researchers using a synchrotron X-ray beamline or an in-house micro-CT scanner. The same data set has been used to investigate various pore-scale flow and transport processes in natural porous media (Blunt et al., 2013; Muljadi et al., 2016). The data set is freely accessible via an online portal (Bijeljic & Raeini, 2015). The 3D images represent the internal pore spaces of the digital rock cores. In particular, we use three sets of 3D images of Bentheimer sandstone,

19447973, 2023, 12, Downloaded from https://agupubs.onlinelibrary.wiley.com/doi/10.1029/2023WR035064 by Cochrane Canada Provision, Wiley Online Library on [28/12/2023]. See the Terms and Conditions (https://onlinelibrary.wiley.com/terms-and-conditions) on Wiley Online Library for rules of use; OA articles are governed by the applicable Creative Commons License

Berea sandstone, and Ketton limestone cores. The Bentheimer sandstone and the Ketton limestone images are 1,000 × 1,000 × 1,000 cubic voxels in size with a resolution of 3 μm/voxel, while the Berea sandstone core is 400 × 400 × 400 cubic voxels in size with a resolution of 5.3 μm/voxel. To unify the scale of all samples in our study, we rescale the Berea sandstone images to 712 × 712 × 712 cubic voxels, such that each voxel corresponds to a physical dimension of 3 μm. By calculating the porosity of the rescaled samples, we found they are within ∼2% of the original sample porosity, which verifies the rescaling technique. Then, we extract subvolumes from the 3D images by applying a sliding cube of 150 × 150 × 150 cubic voxels with an overlapping stride of 50 voxels (Table 1).

We numerically determine the subvolumes' permeabilities using OpenFOAM®, which is an open-source set of solvers for CFD simulations (Horgue et al., 2015). We employ OpenFOAM® to model incompressible steady-state viscous flow by solving the Navier-Stokes equation. The pressure and velocity of the fluid flow are solved iteratively using the semi-implicit method for pressure-linked equations algorithm. For each subvolume, we simulate water flow along each of the principal axes (i.e., $x$, $y$, $z$). We apply a total pressure drop of $\Delta p = 1$ Pa across the bounding surfaces that are normal to the flow direction (i.e., inlet and outlet) and keep the remaining bounding surfaces as no-flow boundaries. The no-slip boundary condition is applied to the solid surfaces in the computational domain. The simulation produces a steady-state velocity field across the entire subvolume. In the end, we compute the volumetric flux $Q$ through the subvolume by integrating the velocities normal to the outlet surface (Equation 1a) and use Darcy's law to get the subvolume's absolute permeability $k$ (Equation 1b).

$$Q_i = \iint u_i dA \tag{1a}$$

$$k_i = \frac{Q_i \mu L}{\Delta p A}, \tag{1b}$$

where $i = x, y, z$ are the principal axes, μ is the dynamic viscosity of water, $L$ is the length of the subvolume, and $A$ is the area of the bounding surface.

We completed over 15,336 permeability simulations of the 150 × 150 × 150 subvolume data set. This data set is subsequently used as the input for the permeability upscaling models. We investigate the porosity $\phi$ and permeability anisotropy $I_a$ of the subvolumes (Figure 1), where $I_a$ is a 3D estimation of the deviation from isotropy (Clavaud et al., 2008).

$$k_{\text{iso}} = (k_{\min} k_{\text{int}} k_{\max})^{\frac{1}{3}}, \tag{2a}$$

$$I_a = \left[ \frac{(k_{\min} - k_{\text{iso}})^2 + (k_{\text{int}} - k_{\text{iso}})^2 + (k_{\max} - k_{\text{iso}})^2}{k_{\min}^2 + k_{\text{int}}^2 + k_{\max}^2} \right]^{\frac{1}{2}}, \tag{2b}$$

where $k_{\text{iso}}$ represents the equivalent isotropic permeability of a given subvolume, and $k_{\min}$, $k_{\text{int}}$, and $k_{\max}$ are its minimum, intermediate and maximum permeabilities, respectively. When referring to geologic porous media, rock samples with $I_a < 0.15$ are considered relatively isotropic, while rock samples with $I_a > 0.4$ are considered highly anisotropic (Clavaud et al., 2008). Our data set comprises of a sizable percentage of highly anisotropic subvolumes and a broad range of $I_a$ values (Figures 1b, 1d, and 1f). This is crucial to make sure the model is broadly applicable to a wide range of heterogeneity and that its usefulness is not limited to isotropic and homogenous samples.

We stitch together every eight neighboring subvolumes to obtain a total of 639 300 × 300 × 300 cubic voxel volumes, which serve as the training data set for the PINN permeability upscaling models (Figure 9). We determine the permeability of the larger samples in three directions using OpenFOAM®. Our data set consists of 1,917 300 × 300 × 300 cubic voxel volumes and 15,336 150 × 150 × 150 cubic voxel subvolumes with labeled permeabilities, which are randomly split into training and testing data sets with a 20–80 split (Figures 2a and 2b).

We also incorporate data augmentation to further increase the size of our data set. Simple image manipulations such as flipping and rotation are commonly used methods for data augmentation in machine learning and they have been used in benchmark data sets including CIFAR-10 and ImageNet (Shorten & Khoshgoftaar, 2019), as well as more recently in digital rock analysis (Elmorsy et al., 2022). To produce four separate subvolumes with the same permeability value, we flip each 2D image slice of each 3D subvolume horizontally and vertically. Then we reverse the ordering of the consecutive 2D image slices to obtain four additional distinct subvolumes with the same permeability value. The data

19447973, 2023, 12, Downloaded from https://agupubs.onlinelibrary.wiley.com/doi/10.1029/2023WR035064 by Cochrane Canada Provision, Wiley Online Library on [28/12/2023]. See the Terms and Conditions (https://onlinelibrary.wiley.com/terms-and-conditions) on Wiley Online Library for rules of use; OA articles are governed by the applicable Creative Commons License

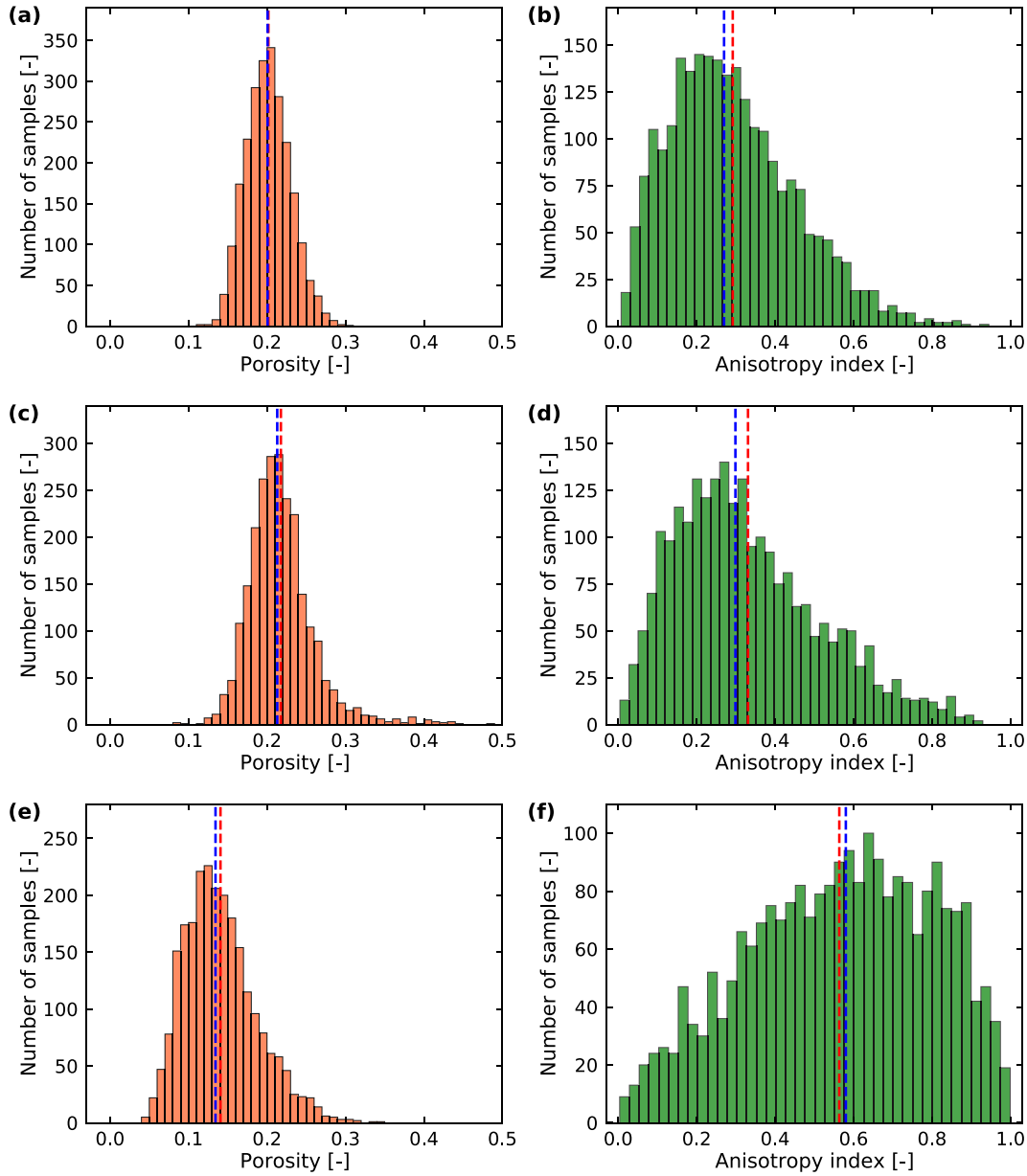


**Figure 1.** The porosity and anisotropy index distributions for the input data set (i.e., 150 × 150 × 150 cubic voxel subvolumes) for the (a, b) Berea sandstone, (c, d) Bentheimer sandstone, and (e, f) Ketton limestone. The porosity ranges from 0.041 to 0.481, and the anisotropy index ranges from ≈0 (i.e., isotropic) to ≈1 (i.e., extremely anisotropic). The blue dashed line and the red dashed line indicate the median and the mean values, respectively.

augmentation process increases the original training data set size by eight times. In the end, we compiled a data set of 12,272 300 × 300 × 300 cubic voxel volumes and 98,176 150 × 150 × 150 cubic voxel subvolumes.

The permeability of the target data set (i.e., 300 × 300 × 300 cubic voxel volumes) ranges from 1,000 to over 5,000 mD, and its distribution is positively skewed with a long tail in the area corresponding to high permeability values (Figures 2a and 2b). The skewness of the data set (i.e., unbalanced) presents a training challenge for machine learning models since they tend to treat the tail area of the distribution as outliers, producing biased predictions that correlate to the most common values in the training data (Bauder & Khoshgoftaar, 2018; Johnson & Khoshgoftaar, 2019; Olson, 2004). Therefore, it is highly challenging for machine learning models to adequately learn from unbalanced data sets (Bauder et al., 2018; Bauder & Khoshgoftaar, 2018). Here, we use the under-sampling technique to transform our data set into a balanced data set (Fernández et al., 2018; Torgo et al., 2015). Specifically, the augmented data set of 300 × 300 × 300 cubic voxel subvolumes is divided into bins that each cover a permeability

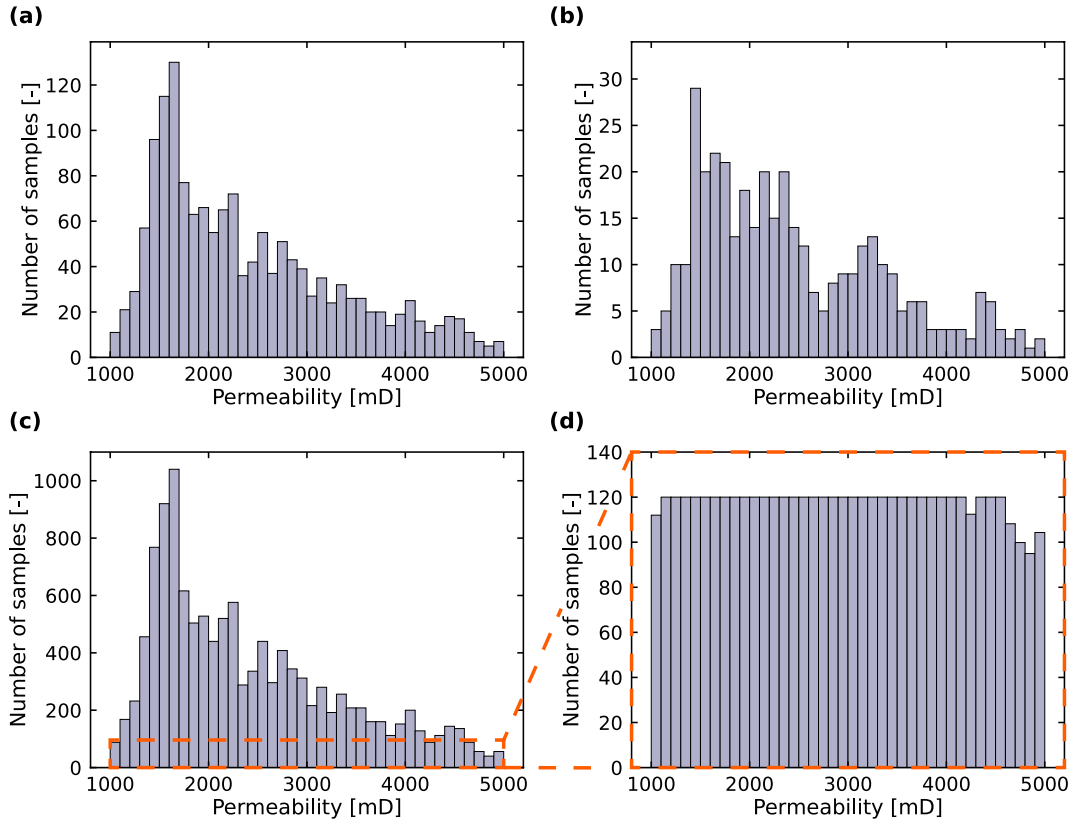


**Figure 2.** Permeability distributions of the (a) training and (b) testing data sets that consist of 300 × 300 × 300 cubic voxel volumes. (c) Permeability distribution of the augmented training data set resembles a log-normal distribution, with a long tail in the region corresponding to high permeability values. (d) We randomly sample 120 subvolumes from each 100 mD interval from the augmented data set in the range between 1,000 and 5,000 mD to construct a balanced data set.

interval of 100 mD, and 120 subvolumes are then randomly chosen from each bin (Figure 2c). Finally, we obtain a uniformly distributed data set with permeability values ranging from 1,000 to 5,000 mD (Figure 2d). We then locate the corresponding 150 × 150 × 150 cubic voxel subvolumes that make up the 300 × 300 × 300 cubic voxel from the balanced data set. We only balance the 300 × 300 × 300 cubic voxel data set since this is the one whose permeability values are used as target labels in training the machine learning model. The permeabilities of the corresponding 150 × 150 × 150 cubic voxel subvolumes are used as input values for the model. During the model training process, the training data set is further split into validation and training subsets with the same 20–80 split ratio.

### 2.2. Analytical Approach

We develop a novel analytical expression to approximate the upscaled permeability of a volume consisting of 2 × 2 × 2 cell blocks with *anisotropic* permeabilities, based on methodologies introduced by Green and Paterson (2007) and King (1989). Specifically, King (1989) utilized the equivalent resistor model to find the upscaled effective permeability of 2 × 2 isotropic cell blocks (Figure 3a):

$$K_{\text{eff(2D)}}(k_1,k_2,k_3,k_4) = 4(k_1+k_3)(k_1+k_4)[k_2k_4(k_1+k_3)+k_1k_3(k_2+k_4)]\times \{[k_2k_4(k_1+k_3)+k_1k_3(k_2+k_4)](k_1+k_2+k_3+k_4)+ 3(k_1+k_2)(k_3+k_4)(k_1+k_3)(k_2+k_4)\}^{-1}. \quad (3)$$

King (1989) could not extend the same graphical scheme to achieve an analytical expression for the upscaled permeability of 2 × 2 × 2 isotropic cell blocks in 3D, since the problem does not result in a simple closed-form expression (King, 1989). Later on, Green and Paterson (2007) used symbolic computation to mathematically solve the graphical scheme to upscale the 2 × 2 × 2 isotropic cell block. However, the exact solution was prohibitively large and too complex to simplify. Specifically, the full analytical expression had 282,844 "+" signs and was impossible to be presented in their paper. To simplify the analytical solution, they introduced an approximation to the 2 × 2 × 2



19447973, 2023, 12, Downloaded from https://agupubs.onlinelibrary.wiley.com/doi/10.1029/2023WR035064 by Cochrane Canada Provision, Wiley Online Library on [28/12/2023]. See the Terms and Conditions (https://onlinelibrary.wiley.com/terms-and-conditions) on Wiley Online Library for rules of use; OA articles are governed by the applicable Creative Commons License

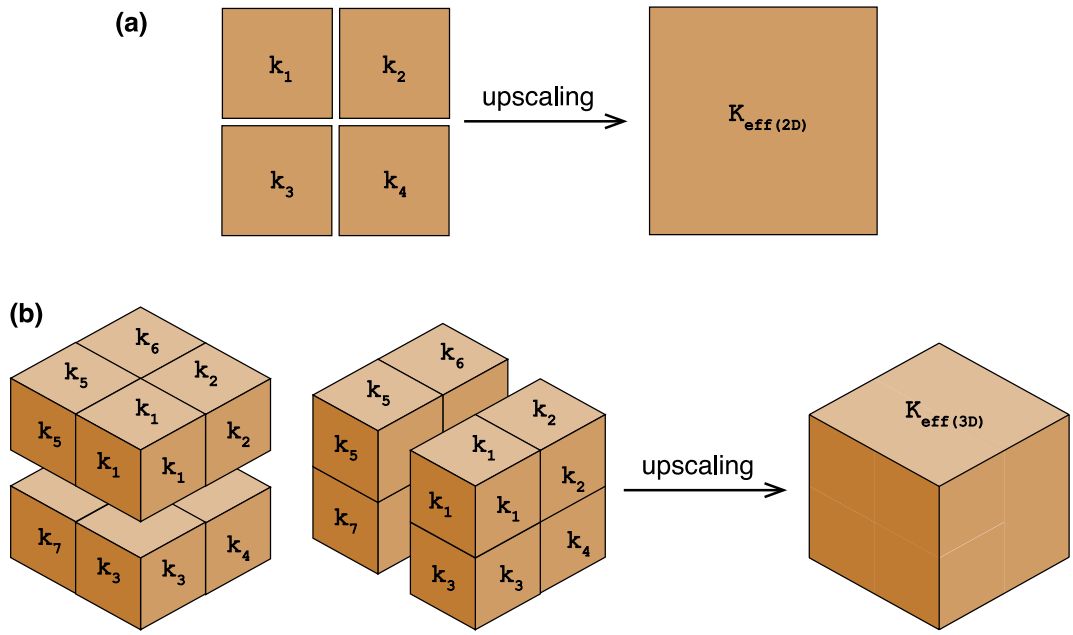


**Figure 3.** (a) 2D upscaling of 2 × 2 isotropic cell blocks introduced by King (1989). (b) Three-dimensional upscaling of 2 × 2 × 2 isotropic cell blocks by first dividing the entire cell block into four 2D cell blocks (i.e., top/bottom and front/back halves). The effective permeability of the entire cell block is approximated as the average of the 2D cell blocks' effective permeabilities (Green & Paterson, 2007).

isotropic cell block problem by assuming that fluid flows from the center of one cell to the center of each adjacent cell. It follows, then, that if the 2 × 2 × 2 cell block is divided into four halves, namely the top/bottom halves and the front/back halves (Figure 3b), the four newly constructed 2 × 2 cell blocks account for all feasible linkages. The effective permeability of each 2 × 2 cell block may be determined using Equation 3. The effective permeability of the 3D 2 × 2 × 2 cell block is then calculated as the average of the four 2D cell blocks' effective permeabilities,

$$K_{\text{eff(3D)}}(k_1,\ldots,k_8) = \frac{1}{4}\Big[K_{\text{eff(2D)}}(k_1,k_2,k_3,k_4) + K_{\text{eff(2D)}}(k_5,k_6,k_7,k_8) + K_{\text{eff(2D)}}(k_5,k_6,k_1,k_2) + K_{\text{eff(2D)}}(k_7,k_8,k_3,k_4)\Big]. \quad (4)$$

Motivated by the resistor model of King (1989) and the simplifying assumption of Green and Paterson (2007), we develop a new upscaling solution to calculate the effective permeability of a 2 × 2 × 2 cell block consisting of *anisotropic* cells using the symbolic computation capabilities of the `SymPy` library in `Python`. Specifically, each cell block can be represented by a cross resistor whose resistance for a given direction is given by $1/k$ (Figure 4a). Since each cell is anisotropic, the resistance is direction-dependent (i.e., $1/k_x \neq 1/k_z$). We then solve the equivalent resistor network of a 2 × 2 *anisotropic* cell block in 2D, where each of the four cell blocks is represented by a cross resistor. We apply a no-flow boundary condition at the top and bottom edges


**Figure 4.** (a) We represent each cell with a cross of unequal resistors (i.e., $1/k_x \neq 1/k_z$). (b) Star-triangle transformation yields an equivalent circuit for three nodes joined by three resistors.



19447973, 2023, 12, Downloaded from https://agupubs.onlinelibrary.wiley.com/doi/10.1029/2023WR035064 by Cochrane Canada Provision, Wiley Online Library on [28/12/2023]. See the Terms and Conditions (https://onlinelibrary.wiley.com/terms-and-conditions) on Wiley Online Library for rules of use; OA articles are governed by the applicable Creative Commons License

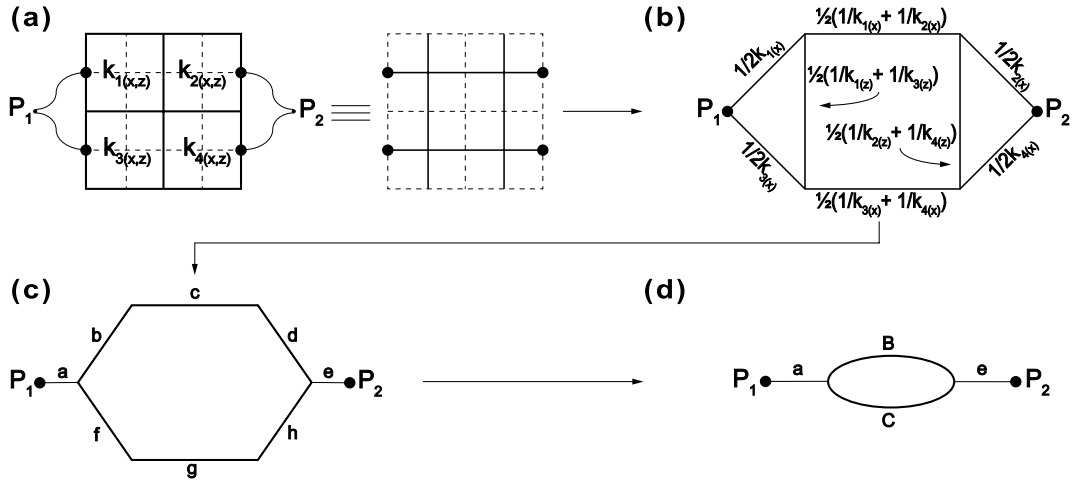


**Figure 5.** (a) The cross resistors representation of a $2 \times 2$ anisotropic cell block. (b) We demonstrate the equivalent resistor network of a $2 \times 2$ anisotropic cell block and (c) illustrates its simplification process using star-triangle transformation. (d) We introduce the final simple resistance network.

and a uniform pressure boundary condition at the left and right edges of the cell block (Figure 5a). We then cut off the dead-end links and bind together the nodes applied with the same pressure (Figure 5b). This resistor network can be further simplified into a circuit of series and parallel resistors using the star-triangle transformation (Figure 5c). The star-triangle transformation is a commonly used transformation in circuit analysis (Kennelly, 1899), and it is illustrated in Figure 4b. The resistances of each link in the newly formed circuit (Figure 5c) are given by:

$$a = \frac{k_{1(z)}k_{3(z)}}{2(k_{1(x)}k_{1(z)}k_{3(x)} + k_{1(x)}k_{1(z)}k_{3(z)} + k_{1(x)}k_{3(x)}k_{3(z)} + k_{1(z)}k_{3(x)}k_{3(z)})}, \tag{5a}$$

$$b = \frac{k_{3(x)}(k_{1(z)} + k_{3(z)})}{2(k_{1(x)}k_{1(z)}k_{3(x)} + k_{1(x)}k_{1(z)}k_{3(z)} + k_{1(x)}k_{3(x)}k_{3(z)} + k_{1(z)}k_{3(x)}k_{3(z)})}, \tag{5b}$$

$$c = \frac{1}{2k_{2(x)}} + \frac{1}{2k_{1(x)}}, \tag{5c}$$

$$d = \frac{k_{4(x)}(k_{2(z)} + k_{4(z)})}{2(k_{2(x)}k_{2(z)}k_{4(x)} + k_{2(x)}k_{2(z)}k_{4(z)} + k_{2(x)}k_{4(x)}k_{4(z)} + k_{2(z)}k_{4(x)}k_{4(z)})}, \tag{5d}$$

$$e = \frac{k_{2(z)}k_{4(z)}}{2(k_{2(x)}k_{2(z)}k_{4(x)} + k_{2(x)}k_{2(z)}k_{4(z)} + k_{2(x)}k_{4(x)}k_{4(z)} + k_{2(z)}k_{4(x)}k_{4(z)})}, \tag{5e}$$

$$f = \frac{k_{1(x)}(k_{1(z)} + k_{3(z)})}{2(k_{1(x)}k_{1(z)}k_{3(x)} + k_{1(x)}k_{1(z)}k_{3(z)} + k_{1(x)}k_{3(x)}k_{3(z)} + k_{1(z)}k_{3(x)}k_{3(z)})}, \tag{5f}$$

$$g = \frac{1}{2k_{4(x)}} + \frac{1}{2k_{3(x)}}, \tag{5g}$$

$$h = \frac{k_{2(x)}(k_{2(z)} + k_{4(z)})}{2(k_{2(x)}k_{2(z)}k_{4(x)} + k_{2(x)}k_{2(z)}k_{4(z)} + k_{2(x)}k_{4(x)}k_{4(z)} + k_{2(z)}k_{4(x)}k_{4(z)})}. \tag{5h}$$

We further simplify the resistor network by combining the resistors in-series into one equivalent resistor, which yields the network shown in Figure 5d. Specifically, resistors b, c, and d combine to form resistor B, and resistors f, g, and h combine to form resistor C. The resistances of B and C are given by,



19447973, 2023, 12, Downloaded from https://agupubs.onlinelibrary.wiley.com/doi/10.1029/2023WR035064 by Cochrane Canada Provision, Wiley Online Library on [28/12/2023]. See the Terms and Conditions (https://onlinelibrary.wiley.com/terms-and-conditions) on Wiley Online Library for rules of use; OA articles are governed by the applicable Creative Commons License

$$B = \frac{k_{3(x)}(k_{1(z)} + k_{3(z)})}{2(k_{1(x)}k_{1(z)}k_{3(x)} + k_{1(x)}k_{1(z)}k_{3(z)} + k_{1(x)}k_{3(x)}k_{3(z)} + k_{1(z)}k_{3(x)}k_{3(z)})} + \frac{k_{4(x)}(k_{2(z)} + k_{4(z)})}{2(k_{2(x)}k_{2(z)}k_{4(x)} + k_{2(x)}k_{2(z)}k_{4(z)} + k_{2(x)}k_{4(x)}k_{4(z)} + k_{2(z)}k_{4(x)}k_{4(z)})} + \frac{1}{2k_{2(x)}} + \frac{1}{2k_{1(x)}} \quad (6a)$$

$$C = \frac{k_{1(x)}(k_{1(z)} + k_{3(z)})}{2(k_{1(x)}k_{1(z)}k_{3(x)} + k_{1(x)}k_{1(z)}k_{3(z)} + k_{1(x)}k_{3(x)}k_{3(z)} + k_{1(z)}k_{3(x)}k_{3(z)})} + \frac{k_{2(x)}(k_{2(z)} + k_{4(z)})}{2(k_{2(x)}k_{2(z)}k_{4(x)} + k_{2(x)}k_{2(z)}k_{4(z)} + k_{2(x)}k_{4(x)}k_{4(z)} + k_{2(z)}k_{4(x)}k_{4(z)})} + \frac{1}{2k_{4(x)}} + \frac{1}{2k_{3(x)}}. \quad (6b)$$

The effective permeability of the $2 \times 2$ *anisotropic* cell block in 2D is then given by

$$K_{\text{eff(2D)}}(k_{1(x,z)}, k_{2(x,z)}, k_{3(x,z)}, k_{4(x,z)}) = \left[ a + \frac{BC}{B + C} + e \right]^{-1}. \quad (7)$$

Finally, we calculate the effective permeability of the top, bottom, left, and right $2 \times 2$ cell blocks in 2D and connect them in parallel in a similar fashion as Green and Paterson (2007) to arrive at the effective permeability of the $2 \times 2 \times 2$ *anisotropic* cell block in 3D,

$$K_{\text{eff(3D)}}(k_{1(x,y,z)}, \ldots, k_{8(x,y,z)}) = \frac{1}{4}\left[K_{\text{eff(2D)}}(k_{5(x,y)}, k_{6(x,y)}, k_{1(x,y)}, k_{2(x,y)}) + K_{\text{eff(2D)}}(k_{5(x,z)}, k_{6(x,z)}, k_{7(x,z)}, k_{8(x,z)}) + K_{\text{eff(2D)}}(k_{7(x,y)}, k_{8(x,y)}, k_{3(x,y)}, k_{4(x,y)}) + K_{\text{eff(2D)}}(k_{1(x,z)}, k_{2(x,z)}, k_{3(x,z)}, k_{4(x,z)})\right]. \quad (8)$$

### 2.3. Physics Informed Neural Network Approach

Physics-informed machine learning is a type of machine learning that combines data and physical models, even in poorly understood, ambiguous, and high-dimensional problems (Karniadakis et al., 2021). Despite the success many machine learning models have achieved in a wide range of applications, purely data-driven models may provide predictions that are physically inconsistent or questionable due to extrapolation or observational biases, which could also impair their ability to be generalized (Karniadakis et al., 2021; Kochkov et al., 2021). As a result, there has been a rising interest in physics-informed learning (Brunton et al., 2020; Dresdner et al., 2022), a method by which previous information derived from our observable, empirical, physical, or mathematical understanding of the universe may be used to improve the performance of a machine learning algorithm (Cuomo et al., 2022). The family of PINNs is a recent example that exemplifies this new learning methodology. PINNs are neural networks that incorporate model equations, like partial differential equations or fractional equations, as a component of the neural network itself (Cai et al., 2021). PINNs are neural networks that incorporate model equations, like partial differential equations or fractional equations, as a component of the neural network itself (Cai et al., 2021). In the context of subsurface applications, PINNs have been recently applied to solve both single-phase and multiphase flow problems (Tartakovsky et al., 2020), as well as solute transport problems (He & Tartakovsky, 2021; Zong et al., 2023).

To physically inform a learning algorithm, observational, learning, or inductive biases are introduced to guide the learning process toward finding solutions that are physically consistent (Karniadakis et al., 2021). Observational biases can be introduced by using data that accurately reflect the underlying physics or through using properly designed data augmentation techniques. Such data may be used to train machine learning systems so that they can learn operators, vector fields, and functions that represent the physical structure of the data (Kashefi et al., 2021). Alternatively, learning biases can be created by selecting suitable loss functions, constraints, and inference algorithms that alter a machine learning model's training phase to explicitly encourage convergence toward solutions that correspond to the underlying physics. The underlying physical rules can only be approximated by employing and modifying soft penalty restrictions. Nonetheless, this approach



19447973, 2023, 12, Downloaded from https://agupubs.onlinelibrary.wiley.com/doi/10.1029/2023WR035064 by Cochrane Canada Provision, Wiley Online Library on [28/12/2023]. See the Terms and Conditions (https://onlinelibrary.wiley.com/terms-and-conditions) on Wiley Online Library for rules of use; OA articles are governed by the applicable Creative Commons License

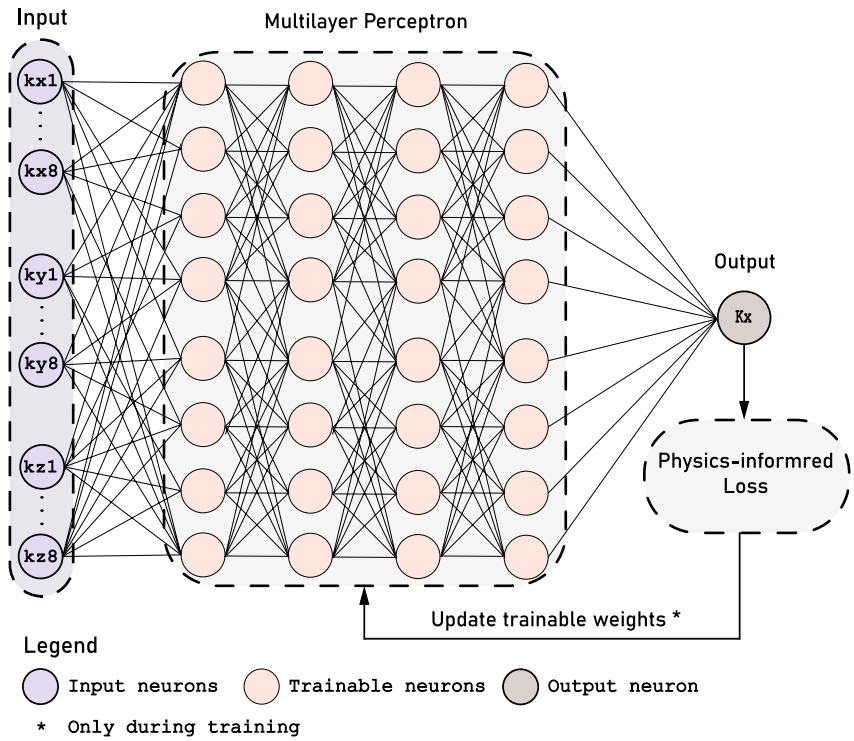


**Figure 6.** The architecture of physics-informed neural network-1 model consists of four dense fully connected layers with eight neurons each in addition to the application of a physics-informed loss function.

provides a very flexible platform for adding a large class of physics-based biases that may be written in the form of integral, differential, or fractional equations (Geneva & Zabaras, 2020; Kissas et al., 2020; Zhu et al., 2019). Lastly, inductive biases related to prior hypotheses that can be incorporated via custom modifications to the machine learning model architecture, ensuring that the predictions implicitly satisfy a given set of physical laws, which are frequently expressed in the form of specific mathematical expressions (Baddoo et al., 2023; Kamrava et al., 2021). Since it enables the rigorous fulfillment of the underlying physical limitations, one may argue that this is the most rational approach to making a learning system physics-informed (Hamzi & Owhadi, 2021; Owhadi & Yoo, 2019). These three paths may be used independently or in combination to expedite the training process and improve the generalizability of physics-informed machine-learning models (Karniadakis et al., 2021).

We develop two physics-informed learning machines by incorporating at least two physical biases into a neural network learning algorithm by combining observational biases with either learning or inductive bias. The observational biases are incorporated in both PINNs by adopting the data augmentation procedure described in the data subsection. For the first neural network (PINN-1), we use a multilayer neural network that consists of an input layer having 24 neurons that receive the permeability values of the eight $150 \times 150 \times 150$ cubic voxel subvolumes in three directions (i.e., $k_x$, $k_y$, $k_z$). The input layer is followed by four fully connected layers with eight neurons each that extract the latent relationships and hidden features through deep learning, which are later used to predict the upscaled permeability of the $300 \times 300 \times 300$ cubic voxel volume in the $x$-direction (i.e., $k_x$) through the final single neuron layer (Figure 6). We note that predicting the upscaled permeability in the $y$- and $z$-direction using the same model is trivial and it only requires rearranging the input subvolume permeabilities. We optimize the network hyper-parameters (i.e., weights and biases) by incorporating a learning bias that adds a soft penalty constraint by minimizing the training loss of the analytical upscaling solution derived above (Equation 8) in addition to the training loss of the observed data. Training the model in this fashion tunes the network hyperparameters such that they approximately satisfy the underlying physical laws (Karniadakis et al., 2021). Specifically, we minimize the following loss function in the training process of PINN-1,

$$\text{loss}_{\text{total}} = \lambda_{\text{data}}\text{loss}_{\text{data}} + \lambda_{\text{anal}}\text{loss}_{\text{anal}}, \quad (9)$$



19447973, 2023, 12, Downloaded from https://agupubs.onlinelibrary.wiley.com/doi/10.1029/2023WR035064 by Cochrane Canada Provision, Wiley Online Library on [28/12/2023]. See the Terms and Conditions (https://onlinelibrary.wiley.com/terms-and-conditions) on Wiley Online Library for rules of use; OA articles are governed by the applicable Creative Commons License

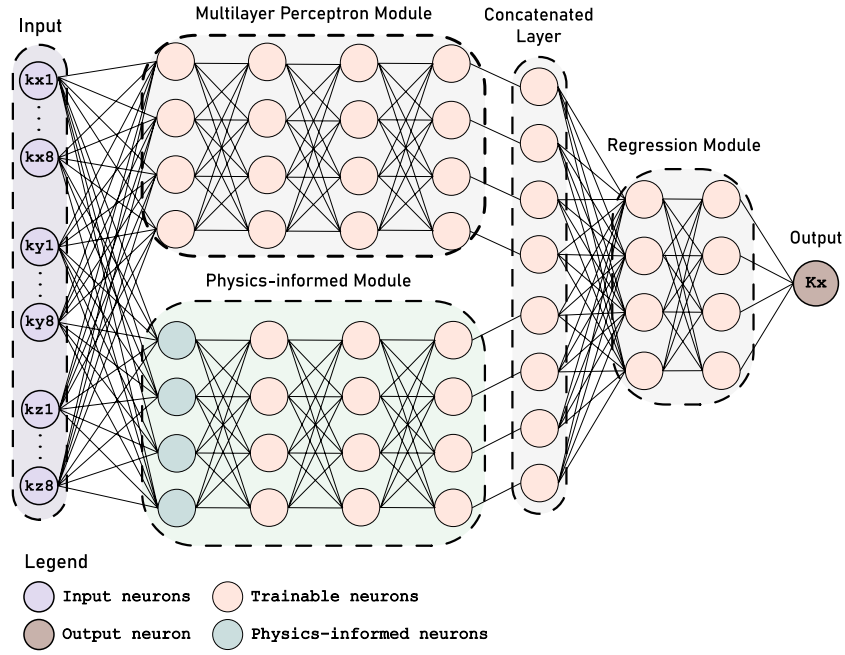


**Figure 7.** The architecture of physics-informed neural network-2 model consists of a multilayer perceptron module and a physics-informed module, both of which have four dense fully connected layers, followed by a concatenation layer and a regression module with two dense fully connected layers. The first layer of the physics-informed module consists of four physics-informed neurons that calculate the effective permeabilities of the top, bottom, left, and right 2 × 2 cell block (Figure 3) using Equation 7.

where $\text{loss}_{\text{data}}$ and $\text{loss}_{\text{anal}}$ are the loss functions corresponding to the data and the analytical solution, respectively, and $\lambda_{\text{data}}$ and $\lambda_{\text{anal}}$ are the corresponding regularization coefficients. Here, we use balanced regularization coefficients ($\lambda_{\text{data}} = \lambda_{\text{anal}} = 1$), which allows the approximate analytical solution to counter overfitting without sacrificing model accuracy gained through training on the data. We calculate the loss functions $\text{loss}_{\text{data}}$ and $\text{loss}_{\text{anal}}$ as the mean absolute relative error (MARE),

$$\text{loss}_i = \frac{\mid k_i - k_{\text{predicted}} \mid}{k_i}, \tag{10}$$

where $k_{\text{predicted}}$ corresponds to the upscaled effective permeabilities predicted by PINN-1.

For the second network PINN-2, we incorporate an inductive bias in addition to the observational bias. Specifically, PINN-2 consists of two parallel neural network modules. The first module is a conventional multilayer network that consists of four fully connected layers with four neurons each, while the second module is a physics-informed multilayer PINN whose first layer consists of four physics-informed neurons (Figure 7). We use lambda layers to enforce the physics-informed neurons to calculate the effective permeabilities of the top, bottom, left, and right 2 × 2 cell block (Figure 3) using Equation 7. Specifically, the first physics-informed neuron calculates the effective permeability of the upper 2 × 2 cell block (i.e., $K_{\text{eff(2D)}}(k_{5(x,y)}, k_{6(x,y)}, k_{1(x,y)}, k_{2(x,y)})$), the second physics-informed neuron calculates the effective permeability of the lower 2 × 2 cell block (i.e., $K_{\text{eff(2D)}}(k_{7(x,y)}, k_{8(x,y)}, k_{3(x,y)}, k_{4(x,y)})$), the third physics-informed neuron calculates the effective permeability of the left 2 × 2 cell block (i.e., $K_{\text{eff(2D)}}(k_{5(x,z)}, k_{6(x,z)}, k_{7(x,z)}, k_{8(x,z)})$), and the fourth physics-informed neuron calculates the effective permeability of the right 2 × 2 cell block (i.e., $K_{\text{eff(2D)}}(k_{1(x,z)}, k_{2(x,z)}, k_{3(x,z)}, k_{4(x,z)})$). The physics-informed layer is then followed by three fully connected layers with four neurons each. The last layers' outputs of both modules are then merged together in a concatenated eight-neuron layer. We then use a regression module consisting of two dense fully connected layers with four neurons each to process the extracted deep features with a dropout rate of 0.1. The final dense layer consists of only a single neuron with a linear activation function that predicts the upscaled permeability of the 300 × 300 × 300 cubic voxel volume in the $x$ direction (i.e., $k_x$) (Figure 7).

We use a regular MARE loss function to train PINN-2



19447973, 2023, 12, Downloaded from https://agupubs.onlinelibrary.wiley.com/doi/10.1029/2023WR035064 by Cochrane Canada Provision, Wiley Online Library on [28/12/2023]. See the Terms and Conditions (https://onlinelibrary.wiley.com/terms-and-conditions) on Wiley Online Library for rules of use; OA articles are governed by the applicable Creative Commons License

$$\text{loss} = \frac{|\ k_{\text{data}} - k_{\text{predicted}}\ |}{k_{\text{data}}}, \tag{11}$$

where $k_{\text{data}}$ corresponds to the true effective permeabilities, and $k_{\text{predicted}}$ corresponds to the effective permeabilities predicted by PINN-2. This approach allows the PINN-2 to automatically find, through model training, the latent relationship between the upper, lower, left, and right 2D halves of the $2 \times 2 \times 2$ cell blocks.

The PINN models are relatively small—PINN-1 has 425 trainable parameters, while PINN-2 has 285 trainable parameters. We train the models using the open-source software interface Keras 2.4.0 and TensorFlow 2.3.1 on NVIDIA GeForce RTX 2080 Ti GPUs. The use of GPUs enables parallel computing that drastically decreases training time and allows the model to scale with more resources (Owens et al., 2008). The Adam optimizer, a computationally efficient extension of adaptive stochastic gradient descent, is utilized for training (Kingma & Ba, 2015). We execute the training process for 100 epochs and store the parameters produced by the best-performing epoch.

## 3. Results and Discussion

We evaluate the accuracy of the upscaling models using the testing data set, which consists of 3,040 $150 \times 150 \times 150$ cubic voxel sub-volumes and their respective 380 $300 \times 300 \times 300$ cubic voxel volumes of multiple rock types. Specifically, we feed the PINN models with the labeled permeability values of the eight $150 \times 150 \times 150$ cubic voxel subvolumes that make up every $300 \times 300 \times 300$ cubic voxel volume in the testing data set. The prediction accuracy is quantified by the relative error RE = $(k_{\text{pred}} - k_{\text{true}})/k_{\text{true}}$ and the absolute relative error (ARE) = |RE|, where $k_{\text{pred}}$ refers to the upscaled permeability predicted by either the PINN models or the analytical solution, and $k_{\text{true}}$ is the permeability values obtained from direct numerical simulation using OpenFOAM®. To avoid the potentially disproportionate influence of outliers, we provide the accuracy only for predictions with AREs within the 95th percentile.

We begin by assessing the accuracy of the analytical solution (Equation 8) in approximating the upscaled permeability of the testing data set. We find that the analytical solution tends to significantly under-predict the upscaled permeability of the larger volumes with some highly inaccurate predictions compared to the true permeabilities (Figure 8a). The analytical solution has a MARE = 0.1542, and it has a wide ARE distribution (|RE| $\in$ [0, 0.5]; Figure 8a). We then assess the accuracy of PINN-1, which is embedded with a physics-informed loss function. We find that the predictions of PINN-1 closely match the true permeabilities over a wide range of permeability values (Figure 8c), though it slightly under-predicts the true permeability. The ARE distribution of PINN-1 reveals that the majority of model predictions are in the low error region (Figure 8d). Additionally, the predictions of PINN-1 have MARE = 0.102, which is significantly lower than that of the analytical solution. Finally, we assess the accuracy of PINN-2, which is embedded with the analytical solution through a physics-informed architecture. We find PINN-2 outperforms both the analytical solution and PINN-1 by achieving a MARE = 0.090. Moreover, PINN-2 delivers balanced predictions over a large range of permeability values (Figure 8c). The superior performance of PINN-2 is attributed to the inductive bias incorporated into the network architecture through the introduction of the analytical solution.

In addition to achieving low error on the testing data set, generalizability is another key metric in evaluating machine learning models. In this context, generalizability is defined as a model's ability to make reasonable predictions when applied to data sets that were not used in the training process (LeCun et al., 2015). Furthermore, we test the model's predictive capability after multiple levels of upscaling. Specifically, we compile a new testing data set comprising of 45 previously unseen $600 \times 600 \times 600$ cubic voxel volumes and their respective 2,880 $150 \times 150 \times 150$ subvolumes for the three rock types (i.e., Berea sandstone, Bentheimer sandstone, and Ketton limestone). The permeabilities of the $150 \times 150 \times 150$ subvolumes are predicted by the 3D CNN model introduced by Elmorsy et al. (2022). The first level of upscaling involves using every eight neighboring $150 \times 150 \times 150$ cubic voxel subvolumes of the testing data set to predict the permeability of the $300 \times 300 \times 300$ cubic voxel subvolumes that encompass them (Figures 9a and 9b). The second level of upscaling uses the predicted permeabilities of the $300 \times 300 \times 300$ cubic voxel subvolumes to yield the permeability of the $600 \times 600 \times 600$ cubic voxel volume (Figures 9b and 9c).

We find that the additional level of upscaling exacerbates the under-prediction error of PINN-1, and its predictions have a MARE = 0.158 (Figure 10a). In contrast, PINN-2 produces highly accurate and balanced predictions after two levels of upscaling over a wide range of permeability values, and its predictions have a much lower



19447973, 2023, 12, Downloaded from https://agupubs.onlinelibrary.wiley.com/doi/10.1029/2023WR035064 by Cochrane Canada Provision, Wiley Online Library on [28/12/2023]. See the Terms and Conditions (https://onlinelibrary.wiley.com/terms-and-conditions) on Wiley Online Library for rules of use; OA articles are governed by the applicable Creative Commons License

10.1029/2023WR035064

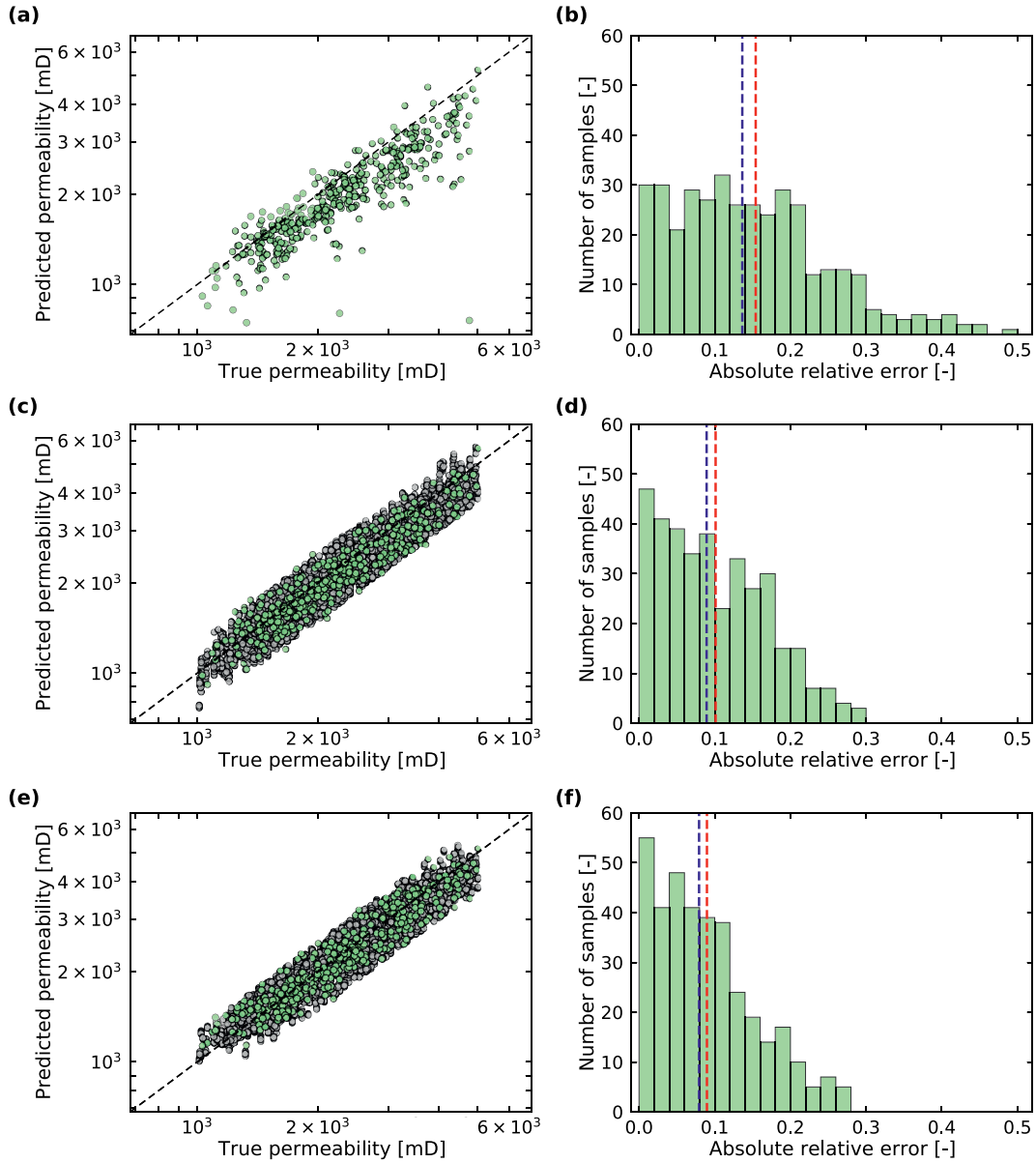


**Figure 8.** Effective permeability prediction of the $300 \times 300 \times 300$ cubic voxel volumes by upscaling $2 \times 2 \times 2$ anisotropic subvolumes of size $150 \times 150 \times 150$ cubic voxels using (a, b) the approximate analytical solution (Equation 8), (c, d) physics-informed neural network-1 (PINN-1) and (e, f) PINN-2. (left column) While the approximate analytical solution significantly under-predicts the true permeabilities obtained from direct numerical simulation, both PINN-1 and PINN-2 achieve excellent accuracy for both the training data set (gray circles) and the testing data set (green circles). The black dashed line represents perfect agreement between the predicted permeability and the true permeability. (right column) The absolute relative error (ARE) of the approximate analytical solution has a wide distribution, while the ARE distributions for both PINNs are much narrower, with the vast majority of the model predictions clustered in the low error range. The vertical blue dashed line and the red dashed line illustrate the median ARE and the mean absolute relative error, respectively.

MARE = 0.062 compared to PINN-1 (Figure 10b). Interestingly, the predictions of PINN-2 are more accurate after two levels of upscaling compared to after just one level of upscaling. Our framework allows for additional levels of upscaling, though we could not demonstrate its accuracy after further upscaling due to the limited availability of larger micro-CT scans and the high computational demand associated with obtaining the true permeabilities of larger samples for comparison.

We note that while direct numerical simulation on a large sample domain is feasible with the advancement in computing power and novel algorithms such as the hybrid multiscale finite volume method (Barajas-Solano &



19447973, 2023, 12, Downloaded from https://agupubs.onlinelibrary.wiley.com/doi/10.1029/2023WR035064 by Cochrane Canada Provision, Wiley Online Library on [28/12/2023]. See the Terms and Conditions (https://onlinelibrary.wiley.com/terms-and-conditions) on Wiley Online Library for rules of use; OA articles are governed by the applicable Creative Commons License

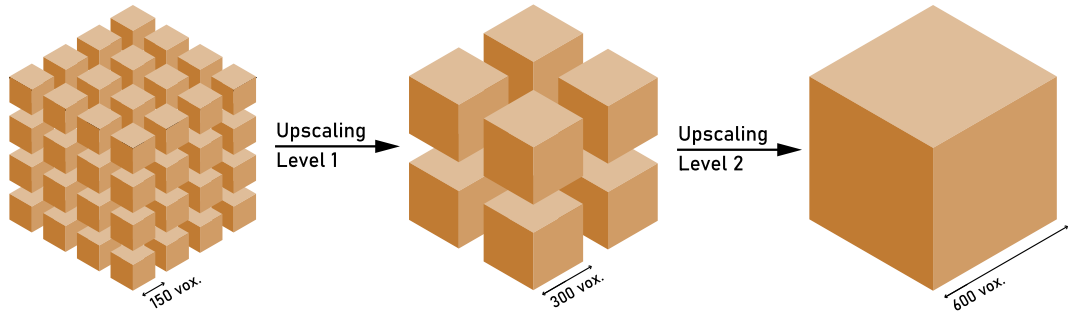


**Figure 9.** Schematic of multiple levels of upscaling by recursively applying the physics-informed neural network models.

Tartakovsky, 2016), they nevertheless remain computationally expensive. For example, solving for the permeability of a single 600 × 600 × 600 cubic voxel volume using OpenFOAM® takes over a day on a server cluster using 32 cores of 3.20 GHz CPUs (~1 sample/day). In contrast, permeability prediction of each 150 × 150 × 150 cubic voxel subvolume using the 3D CNN model (Elmorsy et al., 2022) takes less than 5 ms (~200 samples/second) on a computational cluster with seven GPUs, while both PINN models execute two levels of upscaling to achieve the permeability of the 600 × 600 × 600 cubic voxel volume in less than 400 milliseconds (~2.5 samples/second) on a single 3.20 GHz CPU. Therefore, the machine learning framework presented here enables permeability prediction of large digital porous media that is substantially more efficient compared to direct numerical simulation.

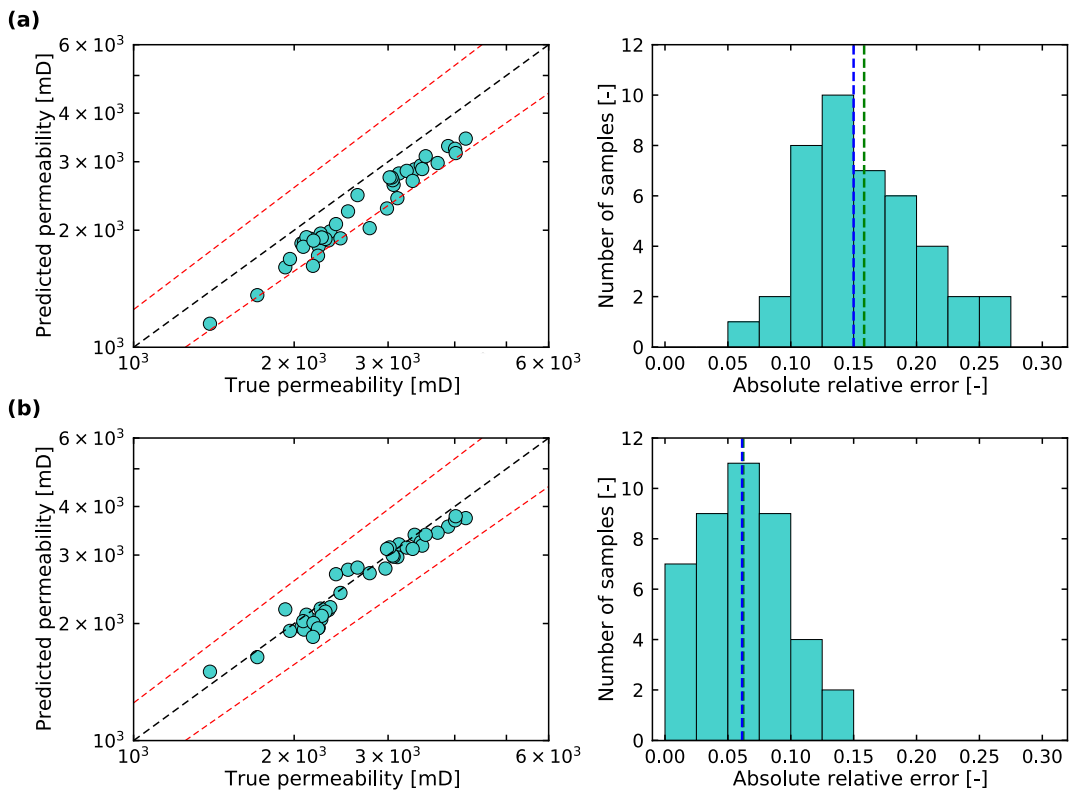


**Figure 10.** Effective permeability prediction of the 600 × 600 × 600 cubic voxel subvolumes by (a) physics-informed neural network-1 (PINN-1) and (b) PINN-2 after two levels of upscaling. Left column: While PINN-1 significantly under-predicts the true permeabilities, PINN-2 achieves accurate and balanced predictions over a large range of permeability values. The black dashed line represents perfect agreement between the predicted permeability and the true permeability, while the red dashed lines represent the boundaries of a 25% mean absolute relative error (MARE) range. Right column: The absolute relative errors (AREs) of predictions produced by PINN-1 are centered around 15%. The AREs of PINN-2's predictions are much lower, and they are clustered around 5%. The vertical blue dashed line and the green dashed line illustrate the median ARE and the MARE, respectively.



19447973, 2023, 12, Downloaded from https://agupubs.onlinelibrary.wiley.com/doi/10.1029/2023WR035064 by Cochrane Canada Provision, Wiley Online Library on [28/12/2023]. See the Terms and Conditions (https://onlinelibrary.wiley.com/terms-and-conditions) on Wiley Online Library for rules of use; OA articles are governed by the applicable Creative Commons License

19447973, 2023, 12, Downloaded from https://agupubs.onlinelibrary.wiley.com/doi/10.1029/2023WR035064 by Cochrane Canada Provision, Wiley Online Library on [28/12/2023]. See the Terms and Conditions (https://onlinelibrary.wiley.com/terms-and-conditions) on Wiley Online Library for rules of use; OA articles are governed by the applicable Creative Commons License

## 4. Conclusions

We have developed three upscaling models for predicting the effective permeability of large digital rock samples based on their smaller constituents. Specifically, we derive a novel analytical solution that approximates the effective permeability of a 3D porous medium consisting of $2 \times 2 \times 2$ *anisotropic* subvolumes (Equation 8). The analytical solution is based on the physical analogy between Darcy's law and Ohm's law, which allows us to find the upscaled permeability by building an equivalent circuit resistor network. In addition, we incorporate the analytical solution into two types of PINN models, where the first model (PINN-1) utilizes a physics-informed loss function (Figure 6), and the second model (PINN-2) encompasses a physics-informed module directly in its architecture (Figure 7).

To assess the accuracy of the upscaling models, we compile a large and diverse input data set of 38,400 $150 \times 150 \times 150$ cubic voxel subvolumes and a target data set of 4,800 $300 \times 300 \times 300$ cubic voxel volumes taken from CT scans of different rock types including Bentheimer sandstone, Berea sandstone, and Ketton limestone. The input data set contains a significant portion of highly anisotropic subvolumes (Figure 1) with permeabilities ranging from 1,000 to 5,000 mD (Figures 2a and 2b). We further conduct data augmentation to enlarge the data set size (Figure 2c) and data balancing to minimize the data set distribution bias (Figure 2d). Both PINN models achieve superior accuracy compared to the analytical solution (Figure 8). Specifically, PINN-1 and PINN-2 achieve MARE = 0.102 and MARE = 0.090, respectively, while the analytical solution yields MARE = 0.15. We further test the capability of the models by applying them to predict the effective permeability of previously unseen $600 \times 600 \times 600$ cubic voxel volumes based on $150 \times 150 \times 150$ cubic voxel subvolumes (i.e., two levels of upscaling), where the permeabilities of the $150 \times 150 \times 150$ cubic voxel subvolumes are predicted by the 3D CNN model previously developed by the authors. We find that the additional level of upscaling *decreases* the accuracy of both the analytical solution and PINN-1, while PINN-2 *increases* its prediction accuracy and achieves MARE = 0.062 after two levels of upscaling (Figure 10). In addition to its accuracy, a key advantage of this framework (i.e., 3D CNN coupled with PINN) is its computational efficiency, since it does not involve any direct numerical simulation.

Recent developments in machine learning methods such as 3D CNN have proven to be important tools in predicting the permeability of digital rock samples. However, existing 3D CNNs are limited in the size of the sample that they can predict, which are typically much smaller than the micro-CT image of the rock sample. The PINN developed here (PINN-2) enables accurate and efficient upscaling to predict the effective permeability of large digital rock samples from their smaller constituents. Together with advances in X-ray micro-CT technologies that can accommodate larger samples, our work paves the way for real time, end-to-end digital rock characterization at the core-scale, a step that will propel tackling key grand challenges pertaining to the sustainable extraction of hydrocarbons, permanent geological sequestration of carbon dioxide, and seasonal storage of renewable energy underground.

## Data Availability Statement

The freely accessible data from the Imperial College London online repository portal (Bijeljic & Raeini, 2015) were used in the creation of this article. Numerical simulations of the 3D porous media samples were conducted using OpenFOAM®, which is an open-source set of solvers for CFD simulations (Horgue et al., 2015). The analytical solutions are developed using the symbolic computation solver SymPy 1.10.1 in Python 3.9.12. We train the machine learning model using the open-source software interface Keras 2.4.0 and TensorFlow 2.3.1 on NVIDIA GeForce RTX 2080 Ti GPUs. Figures were made with Matplotlib 3.5.1, available under the Matplotlib license at https://matplotlib.org/. Part of the software (v.1.1) associated with this article for data processing and machine learning model is publicly available on GitHub https://github.com/elmorsym1 and published on Zenodo, a general-purpose open-access repository (Elmorsy, 2023).

**Acknowledgments**
This research was supported by the Natural Sciences and Engineering Research Council of Canada (NSERC) Discovery Grants (Grant RGPIN-2019-07162) and through the Canadian Nuclear Energy Infrastructure Resilience under Systemic Risk (CaNRisk)—Collaborative Research and Training Experience (CREATE). Additional support by the INViSionLab of McMaster University is gratefully acknowledged. A patent has been filed to protect the developed algorithm.

## References

Alqahtani, N. J., Chung, T., Wang, Y. D., Armstrong, R. T., Swietojanski, P., & Mostaghimi, P. (2021). Flow-based characterization of digital rock images using deep learning. *SPE Journal*, *26*(4), 1–12. https://doi.org/10.2118/205376-pa

Andrä, H., Combaret, N., Dvorkin, J., Glatt, E., Han, J., Kabel, M., et al. (2013). Digital rock physics benchmarks—Part II: Computing effective properties. *Computers & Geosciences*, *50*, 33–43. https://doi.org/10.1016/j.cageo.2012.09.008

Baddoo, P. J., Herrmann, B., McKeon, B. J., Nathan Kutz, J., & Brunton, S. L. (2023). Physics-informed dynamic mode decomposition. *Proceedings of the Royal Society A*, *479*(2271), 20220576. https://doi.org/10.1098/rspa.2022.0576

Barajas-Solano, D. A., & Tartakovsky, A. M. (2016). Hybrid multiscale finite volume method for advection-diffusion equations subject to heterogeneous reactive boundary conditions. *Multiscale Modeling and Simulation*, *14*(4), 1341–1376. https://doi.org/10.1137/15M1022537

Bashtani, F., Taheri, S., & Kantzas, A. (2018). Scale up of pore-scale transport properties from micro to macro scale; network modelling approach. *Journal of Petroleum Science and Engineering*, *170*, 541–562. https://doi.org/10.1016/j.petrol.2018.07.001

Bauder, R. A., & Khoshgoftaar, T. M. (2018). The effects of varying class distribution on learner behavior for medicare fraud detection with imbalanced big data. *Health Information Science and Systems*, *6*(1), 9. https://doi.org/10.1007/s13755-018-0051-3

Bauder, R. A., Khoshgoftaar, T. M., & Hasanin, T. (2018). An empirical study on class rarity in big data. In *2018 17th IEEE international conference on machine learning and applications* (pp. 785–790).

Bear, J. (2013). *Dynamics of fluids in porous media*. Courier Corporation.

Bear, J., & Bachmat, Y. (1991). Introduction to modeling phenomena of transport in porous media. In *Theory and applications of transport in porous media*.

Berg, C. F., Lopez, O., & Berland, H. (2017). Industrial applications of digital rock technology. *Journal of Petroleum Science and Engineering*, *157*, 131–147. https://doi.org/10.1016/j.petrol.2017.06.074

Bijeljic, B., & Raeini, A. Q. (2015). Micro-CT images and networks. Retrieved from https://www.imperial.ac.uk/earth-science/research/research-groups/pore-scale-modelling/micro-ct-images-and-networks/

Blunt, M. J. (2001). Flow in porous media—Pore-network models and multiphase flow. *Current Opinion in Colloid & Interface Science*, *6*(3), 197–207. https://doi.org/10.1016/s1359-0294(01)00084-x

Blunt, M. J. (2017). *Multiphase flow in permeable media: A pore-scale perspective*. Cambridge University Press.

Blunt, M. J., Bijeljic, B., Dong, H., Gharbi, O., Iglauer, S., Mostaghimi, P., et al. (2013). Pore-scale imaging and modelling. *Advances in Water Resources*, *51*, 197–216. https://doi.org/10.1016/j.advwatres.2012.03.003

Boek, E. S., & Venturoli, M. (2010). Lattice-Boltzmann studies of fluid flow in porous media with realistic rock geometries. *Computers & Mathematics with Applications*, *59*(7), 2305–2314. https://doi.org/10.1016/j.camwa.2009.08.063

Brunton, S. L., Noack, B. R., & Koumoutsakos, P. (2020). Machine learning for fluid mechanics. *Annual Review of Fluid Mechanics*, *52*(1), 477–508. https://doi.org/10.1146/annurev-fluid-010719-060214

Cai, S., Mao, Z., Wang, Z., Yin, M., & Karniadakis, G. E. (2021). Physics-informed neural networks (PINNS) for fluid mechanics: A review. *Acta Mechanica Sinica*, *37*(12), 1727–1738. https://doi.org/10.1007/s10409-021-01148-1

Cardwell, J. W. T., & Parsons, R. (1945). Average permeabilities of heterogeneous oil sands. *Transactions of the AIME*, *160*(1), 34–42. https://doi.org/10.2118/945034-G

Chen, S., & Doolen, G. D. (1998). Lattice Boltzmann method for fluid flows. *Annual Review of Fluid Mechanics*, *30*(1), 329–364. https://doi.org/10.1146/annurev.fluid.30.1.329

Clavaud, J.-B., Maineult, A., Zamora, M., Rasolofosaon, P., & Schlitter, C. (2008). Permeability anisotropy and its relations with porous medium structure. *Journal of Geophysical Research: Solid Earth*, *113*(B1), B01202. https://doi.org/10.1029/2007jb005004

Cuomo, S., Di Cola, V. S., Giampaolo, F., Rozza, G., Raissi, M., & Piccialli, F. (2022). Scientific machine learning through physics–informed neural networks: Where we are and what's next. *Journal of Scientific Computing*, *92*(3), 88. https://doi.org/10.1007/s10915-022-01939-z

Dong, H., & Blunt, M. J. (2009). Pore-network extraction from micro-computerized-tomography images. *Physical Review E*, *80*(3), 036307. https://doi.org/10.1103/physreve.80.036307

Dresdner, G., Kochkov, D., Norgaard, P., Zepeda-Núñez, L., Smith, J. A., Brenner, M. P., & Hoyer, S. (2022). Learning to correct spectral methods for simulating turbulent flows. arXiv preprint arXiv:2207.00556.

Elmorsy, M. (2023). elmorsym1/Permeability_Upscaling_Via_PINNs: Third Release. Zenodo. https://doi.org/10.5281/zenodo.10158023

Elmorsy, M., El-Dakhakhni, W., & Zhao, B. (2022). Generalizable permeability prediction of digital porous media via a novel multi-scale 3D convolutional neural network. *Water Resources Research*, *58*(3), e2021WR031454. https://doi.org/10.1029/2021wr031454

Fernández, A., Garcia, S., Herrera, F., & Chawla, N. V. (2018). SMOTE for learning from imbalanced data: Progress and challenges, marking the 15-year anniversary. *Journal of Artificial Intelligence Research*, *61*, 863–905. https://doi.org/10.1613/jair.1.11192

Freeze, R. A., & Cherry, J. A. (1979). *Groundwater*. Prentice-Hall.

Geneva, N., & Zabaras, N. (2020). Modeling the dynamics of PDE systems with physics-constrained deep auto-regressive networks. *Journal of Computational Physics*, *403*, 109056. https://doi.org/10.1016/j.jcp.2019.109056

Green, C. P., & Paterson, L. (2007). Analytical three-dimensional renormalization for calculating effective permeabilities. *Transport in Porous Media*, *68*(2), 237–248. https://doi.org/10.1007/s11242-006-9042-y

Hamzi, B., & Owhadi, H. (2021). Learning dynamical systems from data: A simple cross-validation perspective, part I: Parametric kernel flows. *Physica D: Nonlinear Phenomena*, *421*, 132817. https://doi.org/10.1016/j.physd.2020.132817

He, Q., & Tartakovsky, A. M. (2021). Physics-informed neural network method for forward and backward advection-dispersion equations. *Water Resources Research*, *57*(7), e2020WR029479. https://doi.org/10.1029/2020wr029479

Heinemann, N., Alcalde, J., Miocic, J. M., Hangx, S. J. T., Kallmeyer, J., Ostertag-Henning, C., et al. (2021). Enabling large-scale hydrogen storage in porous media—The scientific challenges. *Energy & Environmental Science*, *14*(2), 853–864. https://doi.org/10.1039/d0ee03536j

Horgue, P., Soulaine, C., Fanc, J., Guibert, R., & Debenest, G. (2015). An open-source toolbox for multiphase flow in porous media. *Computer Physics Communications*, *187*, 217–226. https://doi.org/10.1016/j.cpc.2014.10.005

Johnson, J. M., & Khoshgoftaar, T. M. (2019). Survey on deep learning with class imbalance. *Journal of Big Data*, *6*(1), 27. https://doi.org/10.1186/s40537-019-0192-5

Kamrava, S., Sahimi, M., & Tahmasebi, P. (2021). Simulating fluid flow in complex porous materials by integrating the governing equations with deep-layered machines. *NPJ Computational Materials*, *7*(1), 127. https://doi.org/10.1038/s41524-021-00598-2

Karim, M., & Krabbenhoft, K. (2010). New renormalization schemes for conductivity upscaling in heterogeneous media. *Transport in Porous Media*, *85*(3), 677–690. https://doi.org/10.1007/s11242-010-9585-9

Karniadakis, G. E., Kevrekidis, I. G., Lu, L., Perdikaris, P., Wang, S., & Yang, L. (2021). Physics-informed machine learning. *Nature Reviews Physics*, *3*(6), 422–440. https://doi.org/10.1038/s42254-021-00314-5

Kashefi, A., Rempe, D., & Guibas, L. J. (2021). A point-cloud deep learning framework for prediction of fluid flow fields on irregular geometries. *Physics of Fluids*, *33*(2), 027104. https://doi.org/10.1063/5.0033376

Kennelly, A. E. (1899). The equivalence of triangles and three-pointed stars in conducting networks. *Electrical World and Engineer*, *34*(12), 413–414.

King, P. (1989). The use of renormalization for calculating effective permeability. *Transport in Porous Media*, *4*(1), 37–58. https://doi.org/10.1007/bf00134741

Kingma, D. P., & Ba, J. (2015). Adam: A method for stochastic optimization. arXiv preprint.

Kissas, G., Yang, Y., Hwuang, E., Witschey, W. R., Detre, J. A., & Perdikaris, P. (2020). Machine learning in cardiovascular flows modeling: Predicting arterial blood pressure from non-invasive 4D flow MRI data using physics-informed neural networks. *Computer Methods in Applied Mechanics and Engineering*, *358*, 112623. https://doi.org/10.1016/j.cma.2019.112623

Kochkov, D., Smith, J. A., Alieva, A., Wang, Q., Brenner, M. P., & Hoyer, S. (2021). Machine learning–accelerated computational fluid dynamics. *Proceedings of the National Academy of Sciences*, *118*(21), e2101784118. https://doi.org/10.1073/pnas.2101784118



19447973, 2023, 12, Downloaded from https://agupubs.onlinelibrary.wiley.com/doi/10.1029/2023WR035064 by Cochrane Canada Provision, Wiley Online Library on [28/12/2023]. See the Terms and Conditions (https://onlinelibrary.wiley.com/terms-and-conditions) on Wiley Online Library for rules of use; OA articles are governed by the applicable Creative Commons License

Lake, L. W. (1989). *Enhanced oil recovery*. Prentice-Hall.
LeCun, Y., Bengio, Y., & Hinton, G. (2015). Deep learning. *Nature*, *521*(7553), 436–444. https://doi.org/10.1038/nature14539
Manwart, C., Aaltosalmi, U., Koponen, A., Hilfer, R., & Timonen, J. (2002). Lattice-Boltzmann and finite-difference simulations for the permeability for three-dimensional porous media. *Physical Review E*, *66*(1), 1–32. https://doi.org/10.1103/physreve.66.016702
Menke, H. P., Maes, J., & Geiger, S. (2021). Upscaling the porosity–permeability relationship of a microporous carbonate for Darcy-scale flow with machine learning. *Scientific Reports*, *11*(1), 1–10. https://doi.org/10.1038/s41598-021-82029-2
Mostaghimi, P., Blunt, M. J., & Bijeljic, B. (2013). Computations of absolute permeability on micro-CT images. *Mathematical Geosciences*, *45*(1), 103–125. https://doi.org/10.1007/s11004-012-9431-4
Muljadi, B. P., Blunt, M. J., Raeini, A. Q., & Bijeljic, B. (2016). The impact of porous media heterogeneity on non-Darcy flow behaviour from pore-scale simulation. *Advances in Water Resources*, *95*, 329–340. https://doi.org/10.1016/j.advwatres.2015.05.019
Olson, D. L. (2004). Data set balancing. In *Chinese academy of sciences symposium on data mining and knowledge management* (pp. 71–80).
Orr, F. M., Jr., & Taber, J. J. (1984). Use of carbon dioxide in enhanced oil recovery. *Science*, *224*(4649), 563–569. https://doi.org/10.1126/science.224.4649.563
Owens, J. D., Houston, M., Luebke, D., Green, S., Stone, J. E., & Phillips, J. C. (2008). GPU computing. *Proceedings of the IEEE*, *96*(5), 879–899. https://doi.org/10.1109/jproc.2008.917757
Owhadi, H., & Yoo, G. R. (2019). Kernel flows: From learning kernels from data into the abyss. *Journal of Computational Physics*, *389*, 22–47. https://doi.org/10.1016/j.jcp.2019.03.040
Shorten, C., & Khoshgoftaar, T. M. (2019). A survey on image data augmentation for deep learning. *Journal of Big Data*, *6*(1), 1–48. https://doi.org/10.1186/s40537-019-0197-0
Siavashi, J., Najafi, A., Ebadi, M., & Sharifi, M. (2022). A CNN-based approach for upscaling multiphase flow in digital sandstones. *Fuel*, *308*, 122047. https://doi.org/10.1016/j.fuel.2021.122047
Spanne, P., Thover, J. F., Jacquin, C. J., Lindquist, W. B., Jones, K. W., & Adler, P. M. (1994). Synchrotron computed microtomography of porous media: Topology and transports. *Physical Review Letters*, *73*(14), 2001–2004. https://doi.org/10.1103/physrevlett.73.2001
Szulczewski, M. L., MacMinn, C. W., Herzog, H. J., & Juanes, R. (2012). Lifetime of carbon capture and storage as a climate-change mitigation technology. *Proceedings of the National Academy of Sciences*, *109*(14), 5185–5189. https://doi.org/10.1073/pnas.1115347109
Tahmasebi, P., Kamrava, S., Bai, T., & Sahimi, M. (2020). Machine learning in geo- and environmental sciences: From small to large scale. *Advances in Water Resources*, *142*, 103619. https://doi.org/10.1016/j.advwatres.2020.103619
Tartakovsky, A. M., Marrero, C. O., Perdikaris, P., Tartakovsky, G. D., & Barajas-Solano, D. (2020). Physics-informed deep neural networks for learning parameters and constitutive relationships in subsurface flow problems. *Water Resources Research*, *56*(5), e2019WR026731. https://doi.org/10.1029/2019wr026731
Torgo, L., Branco, P., Ribeiro, R. P., & Pfahringer, B. (2015). Resampling strategies for regression. *Expert Systems*, *32*(3), 465–476. https://doi.org/10.1111/exsy.12081
Wang, Y. D., Chung, T., Armstrong, R. T., McClure, J. E., & Mostaghimi, P. (2019). Computations of permeability of large rock images by dual grid domain decomposition. *Advances in Water Resources*, *126*, 1–14. https://doi.org/10.1016/j.advwatres.2019.02.002
Wei, S., Shen, J., Yang, W., Li, Z., Di, S., & Ma, C. (2019). Application of the renormalization group approach for permeability estimation in digital rocks. *Journal of Petroleum Science and Engineering*, *179*, 631–644. https://doi.org/10.1016/j.petrol.2019.04.057
Xu, Q., Guan, L., Zhang, W., Shi, L., Shao, H., Wang, G., & Long, W. (2022). Multiscale digital rock imaging and modeling for measuring the heterogeneous carbonate and conglomerate permeability at the laboratory plug scale. *Energy & Fuels*, *36*(18), 11025–11039. https://doi.org/10.1021/acs.energyfuels.2c02179
Zhang, H., Ait Abderrahmane, H., Arif, M., Al Kobaisi, M., & Sassi, M. (2022). Influence of heterogeneity on carbonate permeability upscaling: A renormalization approach coupled with the pore network model. *Energy & Fuels*, *36*(6), 3003–3015. https://doi.org/10.1021/acs.energyfuels.1c04010
Zhu, Y., Zabaras, N., Koutsourelakis, P.-S., & Perdikaris, P. (2019). Physics-constrained deep learning for high-dimensional surrogate modeling and uncertainty quantification without labeled data. ArXiv, abs/1901.06314
Zong, Y., He, Q., & Tartakovsky, A. M. (2023). Improved training of physics-informed neural networks for parabolic differential equations with sharply perturbed initial conditions. *Computer Methods in Applied Mechanics and Engineering*, *414*, 116125. https://doi.org/10.1016/j.cma.2023.116125



19447973, 2023, 12, Downloaded from https://agupubs.onlinelibrary.wiley.com/doi/10.1029/2023WR035064 by Cochrane Canada Provision, Wiley Online Library on [28/12/2023]. See the Terms and Conditions (https://onlinelibrary.wiley.com/terms-and-conditions) on Wiley Online Library for rules of use; OA articles are governed by the applicable Creative Commons License